

Spin Pumping of Magnons Coherently Coupled to a Cavity Dark Mode


H. Pan^{1,2,*}, J. Qian,¹ Z. Rao,¹ C.-M. Hu^{2,†} and Z.H. An^{1,3,4,‡}

¹State Key Laboratory of Surface Physics, Department of Physics, Fudan University, Shanghai 200433, China

²Department of Physics and Astronomy, University of Manitoba, Winnipeg R3T 2N2, Canada

³Institute of Nanoelectronic Devices and Quantum Computing, Fudan University, Shanghai 200433, China

⁴Shanghai Qi Zhi Institute, Shanghai 200232, China

 (Received 27 September 2022; revised 7 December 2022; accepted 9 January 2023; published 31 January 2023)

Cavity magnonics provides a versatile platform to tune the photon-magnon interaction bringing about promising applications for quantum information processing. Here, we implement a metamaterial planar cavity to suppress the radiative damping by engineering the symmetry of the cavity configuration. Then, the mode with suppressed radiative damping, i.e., dark mode, is coupled to the magnon mode in a thin yttrium iron garnet film (5 μm), which is detected by performing the reflection measurements and spin-pumping experiment. Pronounced anticrossing of the ferromagnetic resonance and the cavity dark mode is observed, where the largest coupling strength reaches 2.5% of the resonant cavity frequency. In addition, the spin wave resonances along the thickness direction are identified, which enhances the spin-pumping signal when they coalesce with the hybridized cavity-magnon-polariton mode. The dark mode excited by the planar metamaterial cavity leads to an improvement in the coherent manipulation of the spin current.

DOI: [10.1103/PhysRevApplied.19.014075](https://doi.org/10.1103/PhysRevApplied.19.014075)

I. INTRODUCTION

The coherent information transfer between two subsystems is a prerequisite for quantum information processing, as it enables storage, transport, and interfacing of quantum states [1–6]. Cavity magnonics [7], as a hybrid system, has aroused popularity for its potential application in such coherent quantum information processing [8–13]. In cavity magnonics, the ferromagnetic materials characterized by the high spin density [14,15] and low damping [16–19], such as the yttrium iron garnet (YIG) sphere and film, are utilized to create collective spin excitations [20,21]. The collective coupling strength (g_{eff}) of the excitations out of the spin ensemble is enhanced by the square root of the number of spins ($\sqrt{N_s}$), i.e., $g_{\text{eff}} \propto \sqrt{N_s}$ [20,22–24], which enables the coherent coupling between the magnon mode and the cavity photon mode, manifesting itself as anticrossing of their dispersions. Rich achievements have been realized in the hybridized cavity-magnon system, like non-Hermitian phenomena [25–27], nonlinearities [28–32], and cavity-mediated interaction [33–35]. Besides, magnons are widely used in other hybrid systems, based on magnon-phonon [36–38] and magnon-magnon [39–41] interactions.

Experiments in the hybridized cavity-magnon system were usually performed by measuring the transmission or reflection [42,43] of the microwave cavity where a YIG sample was embedded. However, recently, the measurement of the spin-pumping voltage by electrical detection was demonstrated to be another method to explore the physics of the hybridized cavity-magnon system [44]. Generally, spin pumping requires ferromagnet and normal metal heterostructures, such as a Pt strip grown on YIG film gadolinium gallium garnet (GGG) [19]. Under the illumination of microwaves, a spin current is injected into the normal metal by the precessing magnetization in the ferromagnet. Thus, the spin current in the normal metal is converted into a charge current via the inverse spin Hall effect (ISHE) [45,46]. Research about the hybrid system with electrical architecture has promoted the development of cavity magnonics, typical results including manipulation of the pure spin current coherently coupled with the cavity [44], nonlocal spin currents' manipulation in two YIG/Pt samples [47] as well as coherent spin pumping in the YIG/Py bilayer [41]. This electrical detection of spin-pumping voltage [41] enriches the method of studying magnon-magnon coupling physics, which had previously been studied through transmission or reflection measurement [39,40].

In order to realize the practical application of spin pumping in coherently coupled cavity magnonics, the planar cavity characterized by simple fabrication and easy integration is preferable to the three-dimension cavity.

*hpan19@fudan.edu.cn

†hu@physics.umanitoba.ca

‡anzhenghua@fudan.edu.cn

However, the planar cavity is usually open and therefore has inevitably significant radiative (extrinsic) damping. A natural question then arises, can one suppress the extrinsic damping to improve the planar cavity quality.

Motivated by this, we propose a metamaterial planar cavity that can excite dark mode [48] by introducing symmetry breaking of the cavity configuration [48,49], providing a method to suppress the radiative damping [49]. The metamaterials, famous for their freedom to engineer the near-field electromagnetic waves, could be regarded as artificial structures, which are designed and tailored purposely to realize specific functions [50,51]. We study the interaction between the magnon and the cavity mode by placing a Pt/YIG bilayer on the metamaterial planar cavity. The mode volume of the dark mode is minor due to its confinement of electromagnetic field, which enables the ferromagnetic resonance (FMR) and the dark mode to be well spatially overlapped. As a result, they are coherently coupled, with a signature of anticrossing of their dispersions shown in the reflection coefficient and spin-pumping voltage mapping, even though the YIG film is thin. The largest coupling strength between the dark mode and the FMR is up to 2.4% of the resonant cavity frequency. With this thin YIG film, the high-order mode, spin-wave resonance (SWR), is well separated and can thus be identified in the spin-pumping signal, as the spacing of the successive SWRs along the thickness direction is inversely proportional to the squared thickness of the YIG film [52]. We observe that the SWRs enhance the spin-pumping voltage when they coalesce with the hybridized cavity-FMR mode at about an on-resonance frequency. Besides, our setup shows high tunability as the effective magnetic torque can be manipulated continuously, and thereby the coupling strength is continuously controlled. Our work shows that the design flexibility of metamaterial offers compelling advantages in tailoring the cavity magnonics properties, providing a method to improve the manipulation of the spin current in the coherently coupled scenario.

II. THEORETICAL MODEL

Here, we consider a system that mainly incorporates a thin YIG film and a cavity. For the cavity side, microwave resonant modes are excited based on the boundary condition. For the YIG film side, when driven by the uniform alternating magnetic field, conventionally, the fundamental ferromagnetic mode (Kittel mode) is excited with in-phase precessing spins [14]. Besides the uniform FMR mode, the perpendicular standing spin-wave (PSSW) modes appear along the thickness direction as the magnetization is pinned at the surfaces of the YIG film [14,52]. The wave vector of PSSW is perpendicular to the ferromagnetic film plane, and its wavelength is very short due to the thin film. Therefore, the exchange interaction dominates over dipolar

interaction for such spin waves [14,53], whose spectrum can be easily calculated under this condition [14,52].

In such a system, we begin with a model by considering that the FMR and the SWRs are coupled to a common cavity mode, and the interaction among the magnons is ignored. Under a rotating-wave approximation (RWA) [54], the equivalent total Hamiltonian of such hybridized cavity-magnon system reads [55,56]

$$H_{\text{sys}} = \hbar\omega_c\hat{a}^\dagger\hat{a} + \hbar\omega_M\hat{M}^\dagger\hat{M} + \hbar G(\hat{a}^\dagger\hat{M} + \hat{M}^\dagger\hat{a}) + \sum_j \hbar\omega_{m_j}\hat{m}_j^\dagger\hat{m}_j + \sum_j \hbar g_j(\hat{a}^\dagger\hat{m}_j + \hat{m}_j^\dagger\hat{a}), \quad (1)$$

where \hat{a}^\dagger (\hat{a}) stands for the creation (annihilation) operator of the cavity photon at frequency ω_c . \hat{M}^\dagger (\hat{M}) and \hat{m}_j^\dagger (\hat{m}_j) are creation (annihilation) operators for the FMR, and the SWRs at their respective resonance frequency ω_M , ω_{m_j} under the Holstein-Primakoff approximation [57]. G (g_j) is the coupling strength between microwave photons and the FMR (SWR). The parameter j is the order of the SWR.

By adopting the general Langevin equation [54], the dynamic of the cavity photon mode and the FMR, the SWRs can be characterized by the following equations:

$$\frac{d\hat{a}}{dt} = -\frac{i}{\hbar}[\hat{a}(t), H_{\text{sys}}] - \kappa\hat{a}(t) + \sqrt{\kappa}b_{\text{in}} + \sqrt{\kappa}c_{\text{in}}, \quad (2)$$

$$\frac{d\hat{M}}{dt} = -\frac{i}{\hbar}[\hat{M}, H_{\text{sys}}], \quad (3)$$

$$\frac{d\hat{m}_j}{dt} = -\frac{i}{\hbar}[\hat{m}_j, H_{\text{sys}}], \quad (4)$$

where κ represents the extrinsic (radiative) damping of photon mode, and b_{in} , c_{in} correspond to the respective input field from port 1, 2. Suppose that the energy is input from port 1, i.e., $c_{\text{in}} = 0$. In such a case, by substituting Eq. (1) into Eqs. (2)–(4), the dynamic equation of \hat{a} , \hat{M} , \hat{m}_j for our system can be simplified as [56],

$$\frac{d}{dt} \begin{pmatrix} \hat{a} \\ \hat{M} \\ \hat{m}_j \end{pmatrix} = -i \begin{pmatrix} \tilde{\omega}_c & G & g_j \\ G & \tilde{\omega}_M & 0 \\ g_j & 0 & \tilde{\omega}_{m_j} \end{pmatrix} \begin{pmatrix} \hat{a} \\ \hat{M} \\ \hat{m}_j \end{pmatrix} + \begin{pmatrix} \sqrt{\kappa} \\ 0 \\ 0 \end{pmatrix} b_{\text{in}}, \quad (5)$$

where $\tilde{\omega}_c = \omega_c - i\gamma_c$, $\tilde{\omega}_M = \omega_M - i\gamma_M$, $\tilde{\omega}_{m_j} = \omega_{m_j} - i\gamma_{m_j}$, are the complex frequencies of the cavity, the FMR and the SWRs, respectively, and γ_c , γ_M , and γ_{m_j} are their corresponding total damping.

Suppose that the cavity photon mode, the FMR and the SWRs have time dependence of $e^{-i\omega t}$, then the solutions of

Eq. (5) follow as [56]

$$\hat{a} = \frac{i\sqrt{\kappa}b_{\text{in}}}{K}, \quad (6)$$

$$\hat{M} = \frac{i\sqrt{\kappa}b_{\text{in}}}{K} \cdot \frac{G}{\omega - \tilde{\omega}_M}, \quad (7)$$

$$\hat{m}_j = \frac{i\sqrt{\kappa}b_{\text{in}}}{K} \cdot \frac{g_j}{\omega - \tilde{\omega}_{m_j}}, \quad (8)$$

where $K = \omega - \tilde{\omega}_c - (G^2/(\omega - \tilde{\omega}_M)) - \sum_j (g_j^2/(\omega - \tilde{\omega}_{m_j}))$. According to the input-output theory [54], the relation of the input-output field can be described as

$$b_{\text{in}} + b_{\text{out}} = \sqrt{\kappa}\hat{a}, \quad (9)$$

where b_{out} stands for the output field of port 1. Combining the definition of reflection coefficient $S_{11} = b_{\text{out}}/b_{\text{in}}$ and Eqs. (6) and (9), the microwave reflection coefficient can be determined

$$S_{11} = -1 + \frac{i\kappa}{K}. \quad (10)$$

Since the squared modulus of the magnon mode M and m_j correspond to the spin-current response [58], the total spin current I_s incorporates two components, i.e., I_M arising from the FMR and I_{m_j} arising from the SWRs, written as [56,58]

$$I_s = I_M + \sum_j I_{m_j}, \quad (11)$$

$$I_M = \eta_M |M|^2 = \eta_M \left| \frac{\sqrt{\kappa}Gb_{\text{in}}}{K(\omega - \tilde{\omega}_M)} \right|^2, \quad (12)$$

$$I_{m_j} = \eta_{m_j} |m_j|^2 = \eta_{m_j} \left| \frac{\sqrt{\kappa}Gb_{\text{in}}}{K(\omega - \tilde{\omega}_{m_j})} \right|^2, \quad (13)$$

where the parameters η_M and η_{m_j} denote the respective spin-pumping efficiency of the FMR and the SWRs. From Eqs. (12) and (13), we can conclude that the spin-current intensity depends on the coupling nature and the spin-pumping efficiency of the magnon mode.

III. EXPERIMENTAL RESULTS AND DISCUSSION

A. Experimental setup and method

1. Planar cavity

We propose a planar cavity with a metasurface, which can excite a highly confined mode induced by symmetry breaking. The symmetry breaking of the planar cavity arises from the asymmetric locations of two identical bent bars. They are located on each side of two feeding lines with different separations, i.e., $d_1 \neq d_2$ (see Appendix A

for the definition of d_1 and d_2). The dimension of the planar cavity with the two bent bars printed on a Rogers-5880 substrate [see Fig. 1(a)], is further clarified in Appendix A.

With this symmetry-broken planar cavity, the bright and dark modes [48,59] are excited at 2.79 and 3.12 GHz, respectively, as seen in the reflection coefficient spectra in Fig. 1(b). For the bright mode, the currents in the two bent bars oscillate in phase [see Fig. 1(c)] and scatter the electromagnetic field into the free space significantly. In contrast, for the dark mode, the currents in the two bars oscillate out of phase [see Fig. 1(d)] with almost the same amplitude current. This out-of-phase oscillation suppresses the electric and magnetic dipole radiation of the currents oscillating in the two bars. Extracted from the bare-cavity reflection coefficient with the analytical Fano interference model [60], the radiative damping of the bright and dark modes are 142.3 and 2.6 MHz, and the intrinsic damping of the two modes, induced by Ohmic loss, is 1 MHz.

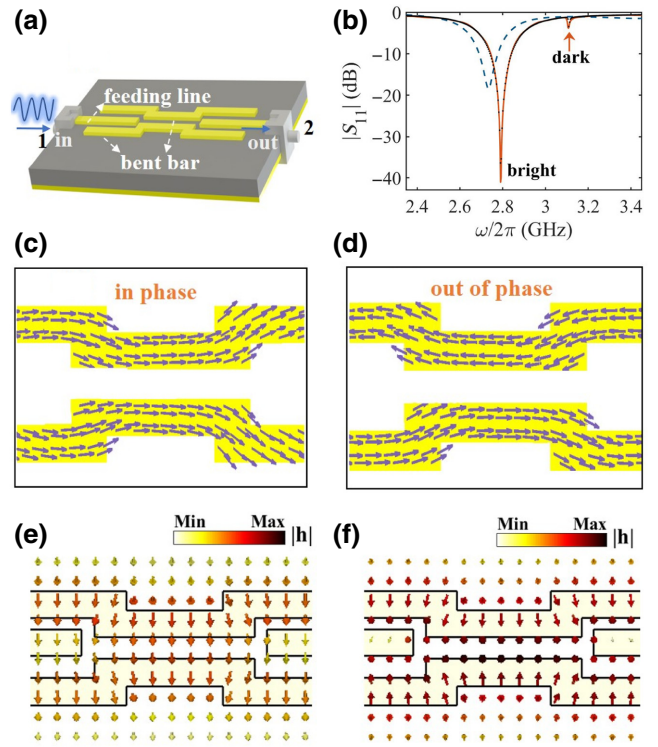


FIG. 1. (a) Sketched structure of the planar cavity with symmetry breaking. A pair of copper bent bars (yellow) are printed on the Rogers-5880 substrate (gray). The microwave is fed to the cavity via the feeding lines. (b) The orange curve represents the measured reflection coefficient spectra of the bare cavity. It is characterized by the radiative bright mode and the confined dark mode marked by an orange arrow. The dashed blue curve denotes the simulated reflection coefficient of symmetrically located bent bars ($d_1 = d_2 = 0.8$ mm). The simulated surface currents in the two bars are (c) in phase and (d) out of phase, representing the signature of the bright and dark modes, respectively. The simulated alternating magnetic field for (e) bright mode and (f) dark mode on the top surface of the cavity.

TABLE I. The quality factors of the frequently applied planar cavities, the corresponding coupled ferromagnets, and the cooperativity between them.

Resonators	$\kappa/2\pi$ (MHz) ^a	Quality factor	Film thickness (dimension)	$\gamma_M/2\pi$ (MHz)	Cooperativity
Split ring [61]	92 (@ 4.78 GHz)	26	(YIG sphere)	/	/
Stripline [56]	10 (@ 4.039 GHz)	200	YIG 83 μm (83 $\mu\text{m} \times 5 \text{ mm} \times 5 \text{ mm}$)	3.5	52.8
Cross line [62]	880 (@ 4.724 GHz)	2.7	(YIG sphere)	/	/
Stubline [63]	32 (@ 4.75 GHz)	74	YIG 9 μm (9 $\mu\text{m} \times 4 \text{ mm} \times 7 \text{ mm}$)	3.25	38.8
ISRR ^b [64]	74 (@3.7 GHz)	25	YIG 25 μm (25 $\mu\text{m} \times 3.7 \text{ mm} \times 3.7 \text{ mm}$)	1.18	23
SCR ^c A [65]	1.05 (@ 5.253 GHz)	2501	Py 10 nm (10 nm \times 40 $\mu\text{m} \times$ 2 μm)	122	43.3
SCR B [66]	2 (@ 5.069 GHz)	1267	Py 30 nm (30 nm \times 14 $\mu\text{m} \times$ 900 μm)	178	65
Our cavity	2.6 (@ 3.12 GHz)	433	YIG 5 μm (5 $\mu\text{m} \times 5 \text{ mm} \times 10 \text{ mm}$)	3.5	445 ^d

^aThe radiative damping of the cavity mode at the resonant frequency.

^bInverted split ring.

^cSuperconducting resonator.

^dThe cooperativity is 445 when $\theta = 0^\circ$.

The large radiative damping of the bright mode originates from the collective radiation of the dipole, while the small radiative damping of the dark mode stems from the suppressed radiation of the dipole. The quality factor of the bright mode is 11, while that of the dark mode is 433. We compare the quality factors of the frequently applied planar cavities with that of the dark mode in Table I. Notably, the quality of the dark mode is the largest except for the superconducting resonator, which operates only at low temperatures. This result implies that the dark mode has an improved quality factor by suppressing the radiative damping at room temperature.

Due to the suppressed radiation of the dark mode, the electromagnetic fields are weakly scattered and thus almost trapped between the two asymmetric bars. Figures 1(e) and 1(f) show the simulated distributions of alternating magnetic field intensity of the dark mode and the bright mode on the surface of the planar cavity, respectively. The distributions demonstrate that the energy of the dark mode is highly confined between the two bent bars, leading to a minor mode volume, which is beneficial to spatial overlap between the cavity mode and the magnon mode. This improved spatial overlap can enhance the interaction between the cavity and the magnon mode.

Significantly, the dark mode is prohibited in a perfectly symmetric structure [48,49]. Therefore, it cannot be excited by a symmetric structure. This can be verified by the simulated result indicated by the dashed curve in Fig. 1(b), which shows that the response of the structure with symmetrically located bars is free from dark mode. This result also evidences that the excitation of the dark mode is permitted by symmetry breaking of the cavity configuration.

2. Reflection measurement and electrical detection

We experiment by applying Pt/YIG heterostructure where a 5- μm -thick YIG film is grown on (111)-oriented

GGG substrate with dimension 10 mm \times 5 mm \times 0.5 mm. In order to implement electrical detection, a Pt stripe is grown on the YIG with a dimension of 6 mm \times 0.5 $\mu\text{m} \times$ 10 nm to form Pt/YIG heterostructure.

We study the interaction between the cavity and the magnon by putting the sample Pt/YIG/GGG onto the two-dimensional (2D) microwave cavity. The planar cavity is connected with VNA via SMA connectors, so that the microwave reflection is measured as shown in Fig. 2(a). Due to the spin-pumping effect and ISHE, the pumped spin currents I_s are converted into charge currents, and thus a spin-pumping voltage V can be detected in the Pt strip [45,46], with the relation $V \propto I_s$ [56]. The cavity is fed with microwaves provided by the microwave generator with an input power of 25 dBm. A lock-in amplifier is applied to measure the spin-pumping voltage as seen in Fig. 2(b). Here, the microwave generator is modulated with a frequency of 8.33 kHz as a reference for the lock in. As depicted in Fig. 2(a), the static magnetic field generated by two magnets is along the y axis. The planar cavity can be rotated in the x - y plane around the z axis, and θ is defined as the angle between the direction of the static field and the feeding-line orientation.

B. Reflection and spin-pumping voltage

We first focus on the interaction between the dark mode and the magnon mode in the case of $\theta = 90^\circ$, where the feeding-line orientation is perpendicular to the static magnetic field, as displayed in Figs. 2(a) and 2(b). For clarity, the interaction between the bright mode and the magnon mode, and the comparison of the interaction behavior between the dark mode and the bright mode when they are coupled with the magnon mode is discussed in Appendix C. Under the condition of $\theta = 90^\circ$, the alternating magnetic field along the z axis is effective on the nonvanishing magnetic torque, as it is perpendicular to the static field (see Appendix B). Figure 2(c) shows the

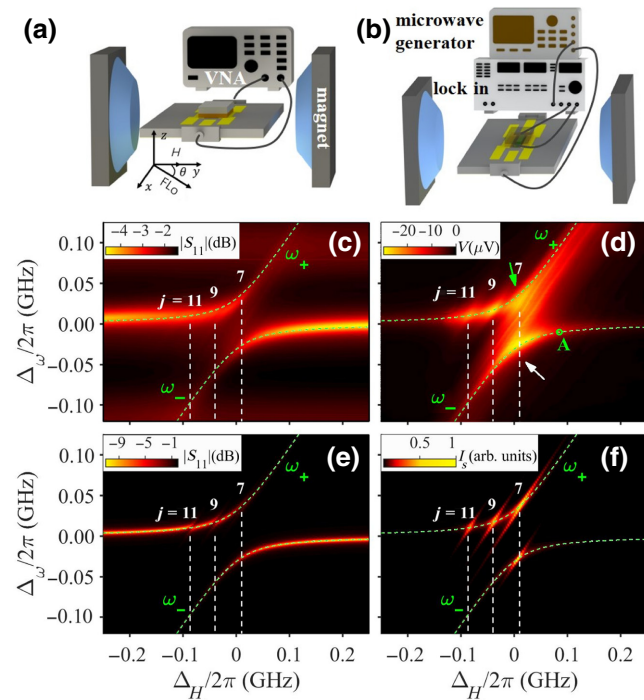


FIG. 2. Illustration of the experimental setup for (a) microwave reflection measurement by applying VNA and (b) electrical detection by applying the lock-in amplifier technique in which the cavity is fed by a microwave generator. FLO is the abbreviation of feeding-line orientation. Experimental (c) reflection coefficient mapping and (d) spin-pumping voltage mapping of the hybridized cavity-magnon system when $\theta = 90^\circ$. (e),(f) are corresponding calculated reflection coefficient and spin-current mapping for the hybridized cavity-magnon system, respectively. The identified SWRs are numbered in (c)–(f). The dispersion of the hybridized cavity-FMR is plotted with green dashed curves in (c)–(f) as visual guidance, which is marked with ω_+ and ω_- . Here, the linewidth of the FMR is $\gamma_M/2\pi = 3.5$ MHz and of the SWR is $\gamma_{m_j}/2\pi = 1.5$ MHz. The coupling strength of the high-order SWRs is $g_j = G/j$ [67,68].

mapping of the reflection coefficient when $\theta = 90^\circ$, which is plotted as a function of the frequency detuning $\Delta_\omega = \omega - \omega_c$ and field detuning $\Delta_H = \omega_M - \omega_c$. An obvious anticrossing of the dispersions of two modes has been observed when the dark mode is hybridized with the FMR, demonstrating the coherent coupling between the FMR and the dark mode. The coupling strength of the cavity dark mode and the FMR is $G/2\pi = 31.2$ MHz. Therefore, the cooperativity is $C = G^2/(\gamma_c\gamma_M) \approx 77$, much larger than 1, further confirming the coherent coupling between the FMR and the dark mode.

Next, we turn to the spin-pumping voltage, the electrically detected response as described in Fig. 2(d). The main anticrossing in the mapping of the spin-pumping voltage originates from the coherent coupling of the dark mode and the FMR. However, the coherently coupled mode

generates modest spin-pumping voltage due to the low spin-pumping efficiency of the FMR [56,67].

Besides the fundamental mode FMR, the additional high-order SWRs along the thickness direction can be resolved in the spin-pumping mapping. As the separation of successive SWRs ($\Delta\omega_m$) is inversely proportional to the squared thickness of YIG film (d) [52], i.e., $\Delta\omega_m \propto (1/d)^2$, the SWRs are well separated by using the thin film, with spacing $\omega_{m_9} - \omega_{m_7} = 0.031$ MHz, $\omega_{m_{11}} - \omega_{m_9} = 0.0383$ MHz, respectively. The above spin waves numbered $j = 7, 9$, and 11 are denoted in Fig. 2(d). With this numbering, the resonant fields of the SWRs approximately abide by the anticipated rule of $|\omega_{m_j} - \omega_{m_1}| = j^2$ [14,22]. Here only odd-numbered modes can be excited due to the selection rule [52,67]. As portrayed in Fig. 2(d), the spin-pumping voltage is enhanced when the SWRs coalesce with the hybridized cavity-FMR mode with ω_+ dispersion [56]. The coalescence occurs at about on-resonance frequency, i.e., $\omega - \omega_c < G$. In order to estimate the magnification induced by the SWR, we compare the maximal spin-pumping voltage induced by 11th SWR V_{11} to that of point A (indicated by the green circle) V_A . Point A and 11th SWR have opposite detuning Δ_H . Our estimation result is $V_{11}/V_A = 2$, implying a twofold enhancement of the spin-pumping signal induced by the SWR. The enhancement induced by the SWRs compensates for the modest spin-pumping signal generated by cavity-magnon-polariton mode, indicated by the green arrow in Fig. 2(d), and thus benefits coherent manipulation of the spin current.

Additionally, we can observe unidentified hybridized SWRs at a field higher than the FMR indicated by a white arrow in Fig. 2(d). These unidentified SWRs can be resolved by reducing the input power to 10 dBm (see Appendix D). They may arise from dipolar interaction, such as magnetostatic backward volume modes. When such SWRs coalesce with the hybridized cavity-FMR mode with dispersion ω_- , the spin-pumping voltage is enhanced.

The behaviors of the hybridized system, including the SWRs, the FMR and the cavity mode, are simulated as shown in Figs. 2(e) and 2(f). The reflection coefficient mapping and spin-current mapping are reproduced with Eqs. (10) and (11), respectively. The simulated FMR to SWRs pumping efficiency ratio is $\eta_M : \eta_{m_7} : \eta_{m_9} : \eta_{m_{11}} : \eta_u = 1 : 7 : 3 : 2 : 1$ (η_u is the spin-pumping efficiency of the unidentified SWR), which implies that the spin-pumping efficiency of the FMR is low.

Then, we set the angle $\theta = 0^\circ$ by aligning the feeding-line orientation parallel to the static magnetic field. Under this condition, the dark mode and the FMR are coherently coupled with a stronger coupling strength $G/2\pi = 74.9$ MHz, compared with the scenario of $\theta = 90^\circ$. The coupling strength is as much as 2.4% of the resonant frequency, near the ultrastrong coupling regime [43,69]. For this configuration, besides the alternating magnetic

field along the z axis, the alternating magnetic field in the x - y plane is also perpendicular to the static field (see Appendix B). This additional effective alternating magnetic field results in increased torque exerted on the magnetization, and therefore the significantly enhanced interaction strength between the dark mode and the FMR. The cooperativity is $C = G^2/(\gamma_c\gamma_M) \approx 445$ when $\theta = 0^\circ$. As shown in Table I, even though the applied YIG film is thinner (or has a smaller volume) than elsewhere [56,63,64], the interaction between the dark mode and the FMR can reach much larger cooperativity. As the FMR dampings differ slightly (see Table I), this superior cooperativity arises dominantly from the advantages of the cavity dark mode, which enhances the magnetic torque and therefore the coupling strength, and also suppresses the radiative damping.

As shown in Figs. 3(a) and 3(b), many nonuniform spin-wave modes are located at the center of the anticrossing, as they are weakly coupled to the cavity mode [70]. These modes with small spacing may originate from the inhomogeneity of the sample [71] or the gradient of the magnetic field [72,73].

C. High tunability

The coupling strength between the dark mode and the FMR could be continuously manipulated in our device by changing the effective magnetic torque. When the cavity together with YIG film is rotated around the z axis from $\theta = 0$ to 90° , the effective magnetic torque decreases, leading to continuously decreasing coupling strength between the dark mode and the FMR, with approximate $\cos\theta$ dependence [see Fig. 4(a)]. It is notable that the coupling strength will not vanish, with minimal coupling strength $G = 31.2$ MHz as marked by an orange arrow in Fig. 4(a). This coupling strength behavior differs from the result in Ref. [74] where the minimal coupling strength approaches 0. As tuning the angle θ from 0 to 90° , the magnetic torque induced by the alternating magnetic field in the x - y plane

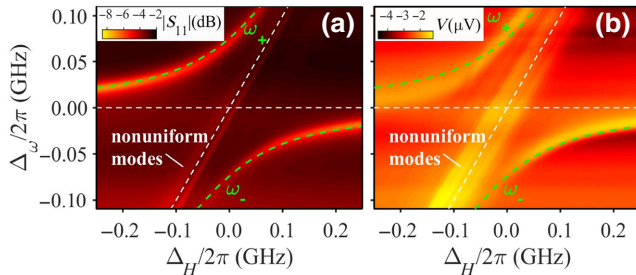


FIG. 3. In the case of $\theta = 0^\circ$, (a),(b) are the experimental reflection coefficient and spin-pumping voltage mapping of the hybridized cavity-magnon system, respectively. The green dashed curves are the calculated dispersion of the hybridized cavity-FMR system. The horizontal and inclined white dashed lines are dispersions of the bare cavity and the FMR, respectively.

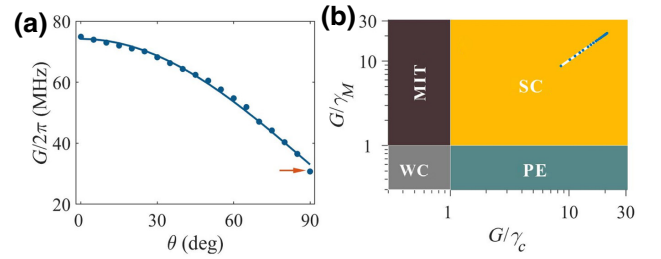


FIG. 4. (a) The coupling strength between the dark mode and the FMR as a function of angle θ plotted with blue symbols. The solid blue line represents the fitted result with the scaling rule $G = (G_0 - G_i) \cos\theta + G_i$, where G_0 (G_i) is the fitted coupling strength at $\theta = 0$ ($\theta = 90^\circ$). An orange arrow denotes the coupling strength at $\theta = 90^\circ$. (b) By continuously tuning the angle θ from 0 to 90° , the interaction between the dark mode and the FMR remains in the strong coupling regime (plotted with logarithmic coordinates).

decreases, while, the magnetic torque induced by the alternating magnetic field along the z axis remains unchanged. This unchanged magnetic torque leads to nonvanishing coupling strength.

Based on the relative strength of G/γ_c and G/γ_M , four coupling regimes are classified as seen in Fig. 4(b). If the coupling strength can overcome all the loss, i.e., $G > \gamma_c$, $G > \gamma_M$, two subsystems are coherently coupled with a signature of anticrossing. The case of $\gamma_M < G < \gamma_c$, $\gamma_c < G < \gamma_M$, $G < \gamma_M$, and $G < \gamma_c$, correspond to magnetically induced transparency (MIT), Purcell effect (PE), weak coupling (WC) regime, respectively [43]. When the coupling strength is manipulated continuously, the interaction between the dark mode and the FMR remains in the strong (coherent) coupling regime [see Fig. 4(b)], despite the fact that the applied YIG film is thin. This coupling behavior arises from two factors: (1) the effective alternating magnetic field of the dark mode has two directions, i.e., in the x - y plane and along the z axis (see Appendix B), contributing to the nonvanishing and continuously manipulated magnetic torque and therefore coupling strength; (2) the dark mode is confined with a small mode volume and a suppressed radiative damping, enabling the coherent coupling between the dark mode and the FMR.

IV. CONCLUSIONS

To summarize, a planar metamaterial cavity is designed to suppress radiative damping by breaking the symmetry of the cavity geometry. With the high-quality planar cavity, even a thin YIG film is allowed to realize coherent coupling between the planar cavity mode (dark mode) and the FMR, whose coupling strength can reach as much as 2.5% of the resonant frequency. With the applied thin film, the high-order mode, i.e., SWRs along the thickness direction are well separated and therefore identified.

The enhancement of the spin-pumping signal is realized at about on-resonance frequency when the SWR coalesces with the hybridized cavity-FMR mode. Our work demonstrates that the design flexibility of metamaterials offers compelling advantages in engineering the properties of the magnetic field, and thus provides promising freedom in the coordination of the cavity magnonics. The method of suppressing the radiation of cavity mode gives rise to an improvement in the coherent manipulation of spin current, which may be useful for quantum information processing in the future [75].

ACKNOWLEDGMENTS

This work is funded by the National Natural Science Foundation of China under Grants No. 12027805 and No. 11991060, and the Shanghai Science and Technology Committee under Grants No. 20JC1414700, No. 20DZ1100604 (Z.H.A.). C.-M.H. acknowledges the support from NSERC Discovery Grants and NSERC Discovery Accelerator Supplements. H. Pan is supported in part by the China Scholarship Council (CSC). The authors thank Mengwen Guo for her helpful suggestions and discussion.

APPENDIX A: THE DIMENSION OF THE PLANAR CAVITY

The planar cavity with detailed dimensions is sketched in Fig. 5(a). It mainly consists of a pair of bent copper bars, printed on the 50 mm × 50 mm × 1.524 mm Rogers-5880 substrate. Two feeding lines are located at the left and right sides of the substrate, respectively. Two bent copper bars are located at the upper and lower sides of the feeding lines with different separations ($d_1 = 0.8$, $d_2 = 1.2$ mm). Therefore, the asymmetry of the cavity configuration is introduced. The substrate is coated with 0.035-mm-thick copper on the bottom layer as grounding.

APPENDIX B: THE MAGNETIC TORQUE

The Pt/YIG/GGG structure is flipped over and fixed on the planar cavity in our setup as seen in Figs. 2(a) and 2(b). When $\theta = 90^\circ$, the effective alternating magnetic field contributing to the magnetic torque is along the z axis as seen in Fig. 5(b). The alternating magnetic field in the x - y plane is negligible as it is parallel to the static magnetic field. When $\theta = 0^\circ$, additional alternating magnetic field in the x - y plane contributes to the magnetic torque as it is perpendicular to the static field [see Fig. 5(c)].

APPENDIX C: COMPARISON BETWEEN DARK MODE AND BRIGHT MODE

The reflection coefficient mappings in the vicinity of the bright-mode resonant frequency are shown in Figs. 6(a)

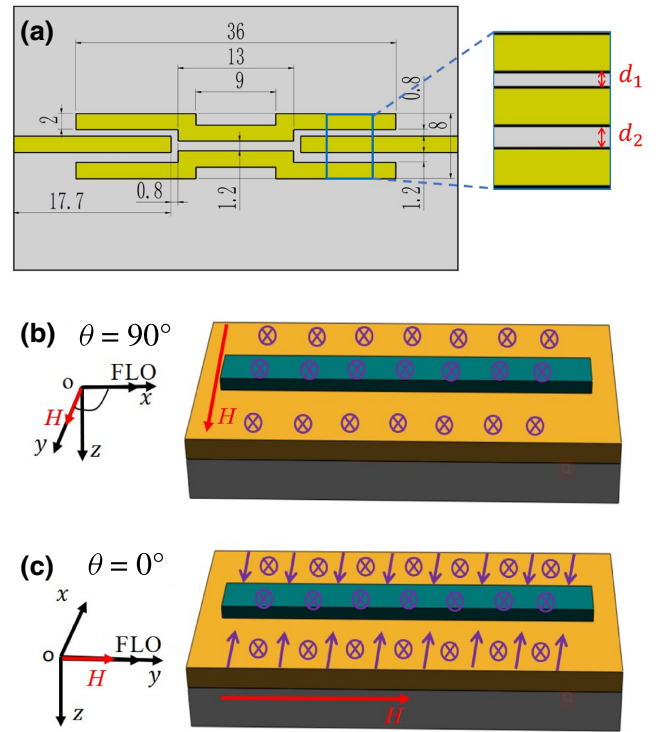


FIG. 5. (a) The dimensions of the planar metamaterial cavity with top projection (unit: mm). (b) When $\theta = 90^\circ$, the effective alternating magnetic field contributing to the magnetic torque is along the z axis. However, the alternating magnetic field in the x - y plane is ineffective (not plotted) as it is parallel to the static magnetic field. (c) When $\theta = 0^\circ$, apart from the alternating magnetic field along the z axis, the alternating magnetic field in the x - y plane (perpendicular to the static magnetic field) also contributes to the magnetic torque. The three-layer structure in (b),(c) is Pt/YIG/GGG (from top to bottom).

and 6(b). At $\theta = 90^\circ$, the dispersions of the bright mode and the magnon mode almost crosses, while, at $\theta = 0^\circ$, the dispersions of the two modes seem to anticross. However, the two modes resulting from interaction are not well separated, as when $\theta = 0^\circ$ the coupling strength between the bright mode and the magnon mode is 67 MHz, which is smaller than the bright-mode damping 143.3 MHz. Therefore, the interaction between the bright mode and the magnon mode is still weak coupling when $\theta = 0$ and 90° .

Besides, the interaction behaviors of the dark modes and the bright mode reflected in the mappings of the spin-pumping voltage, where the frequency range covers both the cavity dark mode and bright mode at both $\theta = 0$ and 90° , are shown in Figs. 6(c) and 6(d). The dispersion of the cavity bright mode intersects that of the magnon mode at both $\theta = 0$ and 90° . This feature implies that the bright mode and the magnon mode are weakly coupled. When $\theta = 0^\circ$, the dispersion behavior in voltage mapping is different from that in the reflection coefficient mapping, where the dispersions of the bright mode and the magnon

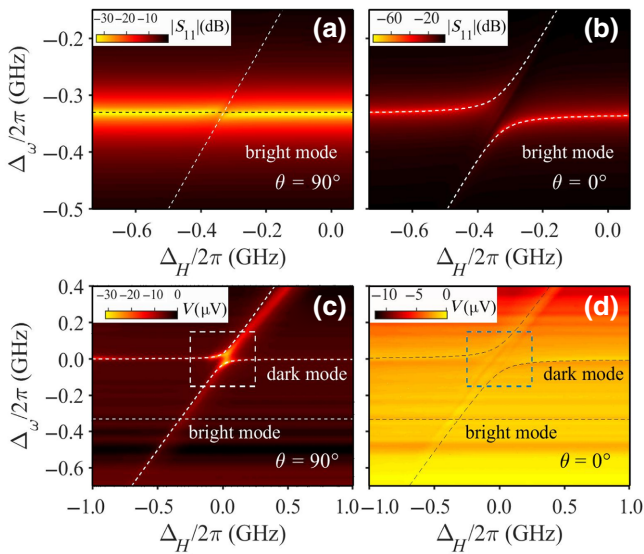


FIG. 6. The measured reflection coefficient mapping in the vicinity of the bright-mode resonant frequency at (a) $\theta = 90^\circ$ and (b) $\theta = 0^\circ$, respectively. The measured spin-pumping voltage mapping, at (c) $\theta = 90^\circ$ and (d) $\theta = 0^\circ$, respectively. Here, the frequency range covers both the dark and bright modes. The areas which are boxed with white and blue dashed lines in the mappings (c),(d) correspond to the interaction between the dark mode and the magnon mode, same as Figs. 2(d) and 2(b). The white and dark dashed curves and lines denote the dispersions. The selective color of the dispersion lines and curves is based on the purpose of distinguishing the dispersion from the mapping.

mode seem to anticross though the coupling strength is smaller than the damping of the cavity bright mode. This means that this kind of weak coupling, whose coupling strength is large while it still can not overcome the mode damping of the subsystem, is not well reflected by electrical detection and its reason remains to be explored. However, the strong-coupling feature can be detected by the reflection and the spin-pumping electrical measurement [44]. Both measurements show the signature of the strong coupling, i.e., the anticrossing of the dispersions of two coupled modes.

In contrast to the bright mode, we clearly observe an anticrossing of the dark mode and the magnon mode at both $\theta = 0$ and 90° , with larger separation at $\theta = 0^\circ$, both in the reflection coefficient and spin-pumping voltage mapping [see Figs. 2(c) and 2(d), 3(a) and 3(b) and 6(c) and 6(d)]. In this case, the coupling strength exceeds both the dampings of the magnon mode and the cavity dark mode, and thus the interaction between the dark mode and the magnon is strong coupling, as clarified in Sec. III. As we demonstrate in Sec. III, the dark mode is localized with small mode volume, leading to large coupling strength and small extrinsic damping, while, the bright mode is radiative with large mode volume, resulting in weak coupling strength and large extrinsic damping. These disparities

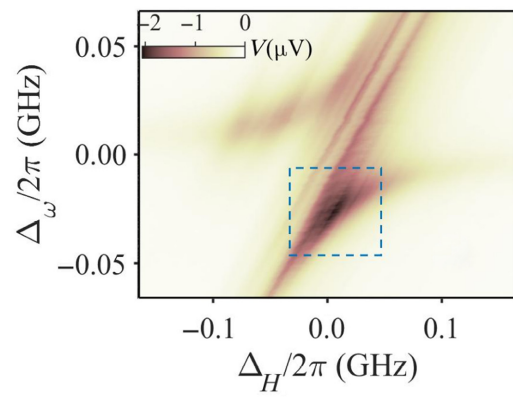


FIG. 7. (a) The measured spin-pumping voltage mapping of the hybridized cavity magnon system when the input microwave power is reduced to 10 dBm at $\theta = 90^\circ$.

account for the strong coupling between the dark mode and the magnon mode, and the weak coupling between the bright mode and the magnon mode.

APPENDIX D: THE SPIN-PUMPING VOLTAGE MEASURED WITH LOW INPUT POWER

Under the low input power, the hybridized cavity-FMR mode with dispersion ω_- is resolved by the evident splits (boxed with blue dashed lines), which stems from the coalescence of the SWRs and the hybridized cavity-FMR mode with dispersion ω_- as seen in Fig. 7(a).

- [1] M. Wallquist, K. Hammerer, P. Rabl, M. Lukin, and P. Zoller, Hybrid quantum devices and quantum engineering, *Phys. Scr.* **T137**, 014001 (2009).
- [2] G. Kurizki, P. Bertet, Y. Kubo, K. Mølmer, D. Petrosyan, P. Rabl, and J. Schmiedmayer, Quantum technologies with hybrid systems, *Proc. Natl. Acad. Sci. USA* **112**, 3866 (2015).
- [3] X. Gu, A. F. Kockum, A. Miranowicz, Y.-x. Liu, and F. Nori, Microwave photonics with superconducting quantum circuits, *Phys. Rep.* **718**, 1 (2017).
- [4] Y. Li, W. Zhang, V. Tyberkevych, W.-K. Kwok, A. Hoffmann, and V. Novosad, Hybrid magnonics: Physics, circuits, and applications for coherent information processing, *J. Appl. Phys.* **128**, 130902 (2020).
- [5] A. J. Heinrich, W. D. Oliver, L. M. Vandersypen, A. Ardavan, R. Sessoli, D. Loss, A. B. Jayich, J. Fernandez-Rossier, A. Laucht, and A. Morello, Quantum-coherent nanoscience, *Nat. Nanotechnol.* **16**, 1318 (2021).
- [6] D. S. Wang, M. Haas, and P. Narang, Quantum interfaces to the nanoscale, *ACS Nano* **15**, 7879 (2021).
- [7] B. Zare Rameshti, S. Viola Kusminskiy, J. A. Haigh, K. Usami, D. Lachance-Quirion, Y. Nakamura, C.-M. Hu, H. X. Tang, G. E. Bauer, and Y. M. Blanter, Cavity magnonics, *Phys. Rep.* **979**, 1 (2022).

- [8] Y. Tabuchi, S. Ishino, A. Noguchi, T. Ishikawa, R. Yamazaki, K. Usami, and Y. Nakamura, Coherent coupling between a ferromagnetic magnon and a superconducting qubit, *Science* **349**, 405 (2015).
- [9] X. Zhang, C.-L. Zou, N. Zhu, F. Marquardt, L. Jiang, and H. X. Tang, Magnon dark modes and gradient memory, *Nat. Commun.* **6**, 1 (2015).
- [10] D. Lachance-Quirion, S. P. Wolski, Y. Tabuchi, S. Kono, K. Usami, and Y. Nakamura, Entanglement-based single-shot detection of a single magnon with a superconducting qubit, *Science* **367**, 425 (2020).
- [11] D. Lachance-Quirion, Y. Tabuchi, A. Gloppe, K. Usami, and Y. Nakamura, Hybrid quantum systems based on magnonics, *Appl. Phys. Express* **12**, 070101 (2019).
- [12] S. Eshete, Quantum information transfer between optical and microwave output modes via cavity magnonics, *J. Magn. Magn. Mater.* **549**, 168987 (2022).
- [13] H. Yuan, Y. Cao, A. Kamra, R. A. Duine, and P. Yan, Quantum magnonics: When magnon spintronics meets quantum information science, *Phys. Rep.* **965**, 1 (2022).
- [14] A. Prabhakar and D. D. Stancil, *Spin Waves: Theory and Applications* (Springer, Berlin, 2009), Vol. 5.
- [15] D. Zhang, X.-M. Wang, T.-F. Li, X.-Q. Luo, W. Wu, F. Nori, and J. You, Cavity quantum electrodynamics with ferromagnetic magnons in a small yttrium-iron-garnet sphere, *npj Quantum Information* **1**, 1 (2015).
- [16] Y. Kajiwara, K. Harii, S. Takahashi, J.-I. Ohe, K. Uchida, M. Mizuguchi, H. Umezawa, H. Kawai, K. Ando, and K. Takanashi, *et al.*, Transmission of electrical signals by spin-wave interconversion in a magnetic insulator, *Nature* **464**, 262 (2010).
- [17] V. Cherepanov, I. Kolokolov, and V. L'vov, The saga of YIG: Spectra, thermodynamics, interaction and relaxation of magnons in a complex magnet, *Phys. Rep.* **229**, 81 (1993).
- [18] A. Serga, A. Chumak, and B. Hillebrands, Yig magnonics, *J. Phys. D Appl. Phys.* **43**, 264002 (2010).
- [19] A. Brataas, B. van Wees, O. Klein, G. de Loubens, and M. Viret, Spin insulatronics, *Phys. Rep.* **885**, 1 (2020).
- [20] A. Imamoglu, Cavity QED based on Collective Magnetic Dipole Coupling: Spin Ensembles as Hybrid Two-Level Systems, *Phys. Rev. Lett.* **102**, 083602 (2009).
- [21] O. O. Soykal and M. E. Flatté, Strong Field Interactions between a Nanomagnet and a Photonic Cavity, *Phys. Rev. Lett.* **104**, 077202 (2010).
- [22] Y. Cao, P. Yan, H. Huebl, S. T. B. Goennenwein, and G. E. W. Bauer, Exchange magnon-polaritons in microwave cavities, *Phys. Rev. B* **91**, 094423 (2015).
- [23] L. V. Abdurakhimov, Y. M. Bunkov, and D. Konstantinov, Normal-Mode Splitting in the Coupled System of Hybridized Nuclear Magnons and Microwave Photons, *Phys. Rev. Lett.* **114**, 226402 (2015).
- [24] M. G. Raizen, R. J. Thompson, R. J. Brecha, H. J. Kimble, and H. J. Carmichael, Normal-Mode Splitting and Linewidth Averaging for Two-State Atoms in an Optical Cavity, *Phys. Rev. Lett.* **63**, 240 (1989).
- [25] M. Harder, L. Bai, P. Hyde, and C.-M. Hu, Topological properties of a coupled spin-photon system induced by damping, *Phys. Rev. B* **95**, 214411 (2017).
- [26] D. Zhang, X.-Q. Luo, Y.-P. Wang, T.-F. Li, and J. You, Observation of the exceptional point in cavity magnon-polaritons, *Nat. Commun.* **8**, 1 (2017).
- [27] Y. Yang, Y.-P. Wang, J. W. Rao, Y. S. Gui, B. M. Yao, W. Lu, and C.-M. Hu, Unconventional Singularity in Anti-Parity-Time Symmetric Cavity Magnonics, *Phys. Rev. Lett.* **125**, 147202 (2020).
- [28] Y.-P. Wang, G.-Q. Zhang, D. Zhang, T.-F. Li, C.-M. Hu, and J. You, Bistability of Cavity Magnon Polaritons, *Phys. Rev. Lett.* **120**, 057202 (2018).
- [29] Y.-P. Wang, G.-Q. Zhang, D. Zhang, X.-Q. Luo, W. Xiong, S.-P. Wang, T.-F. Li, C.-M. Hu, and J. You, Magnon Kerr effect in a strongly coupled cavity-magnon system, *Phys. Rev. B* **94**, 224410 (2016).
- [30] P. Hyde, B. M. Yao, Y. S. Gui, G.-Q. Zhang, J. Q. You, and C.-M. Hu, Direct measurement of foldover in cavity magnon-polariton systems, *Phys. Rev. B* **98**, 174423 (2018).
- [31] R.-C. Shen, Y.-P. Wang, J. Li, S.-Y. Zhu, G. S. Agarwal, and J. Q. You, Long-Time Memory and Ternary Logic Gate using a Multistable Cavity Magnonic system, *Phys. Rev. Lett.* **127**, 183202 (2021).
- [32] H. Pan, Y. Yang, Z. H. An, and C.-M. Hu, Bistability in dissipatively coupled cavity magnonics, *Phys. Rev. B* **106**, 054425 (2022).
- [33] N. J. Lambert, J. A. Haigh, S. Langenfeld, A. C. Doherty, and A. J. Ferguson, Cavity-mediated coherent coupling of magnetic moments, *Phys. Rev. A* **93**, 021803 (2016).
- [34] P.-C. Xu, J. W. Rao, Y. S. Gui, X. Jin, and C.-M. Hu, Cavity-mediated dissipative coupling of distant magnetic moments: Theory and experiment, *Phys. Rev. B* **100**, 094415 (2019).
- [35] B. Zare Rameshti and G. E. W. Bauer, Indirect coupling of magnons by cavity photons, *Phys. Rev. B* **97**, 014419 (2018).
- [36] F. Godejohann, A. V. Scherbakov, S. M. Kukhtaruk, A. N. Poddubny, D. D. Yaremkevich, M. Wang, A. Nadzeyka, D. R. Yakovlev, A. W. Rushforth, A. V. Akimov, and M. Bayer, Magnon polaron formed by selectively coupled coherent magnon and phonon modes of a surface patterned ferromagnet, *Phys. Rev. B* **102**, 144438 (2020).
- [37] C. Berk, M. Jaris, W. Yang, S. Dhuey, S. Cabrini, and H. Schmidt, Strongly coupled magnon-phonon dynamics in a single nanomagnet, *Nat. Commun.* **10**, 1 (2019).
- [38] K. An, R. Kohno, A. N. Litvinenko, R. L. Seeger, V. V. Naletov, L. Vila, G. de Loubens, J. Ben Youssef, N. Vukadinovic, G. E. W. Bauer, A. N. Slavina, V. S. Tiberkevich, and O. Klein, Bright and Dark States of Two Distant Macrospins Strongly Coupled by Phonons, *Phys. Rev. X* **12**, 011060 (2022).
- [39] L. Liensberger, A. Kamra, H. Maier-Flaig, S. Geprägs, A. Erb, S. T. B. Goennenwein, R. Gross, W. Belzig, H. Huebl, and M. Weiler, Exchange-Enhanced Ultrastrong Magnon-Magnon Coupling in a Compensated Ferrimagnet, *Phys. Rev. Lett.* **123**, 117204 (2019).
- [40] J. Chen, C. Liu, T. Liu, Y. Xiao, K. Xia, G. E. W. Bauer, M. Wu, and H. Yu, Strong Interlayer Magnon-Magnon Coupling in Magnetic Metal-Insulator Hybrid Nanostructures, *Phys. Rev. Lett.* **120**, 217202 (2018).
- [41] Y. Li, W. Cao, V. P. Amin, Z. Zhang, J. Gibbons, J. Sklenar, J. Pearson, P. M. Haney, M. D. Stiles, W. E. Bailey, V. Novosad, A. Hoffmann, and W. Zhang, Coherent Spin Pumping in a Strongly Coupled Magnon-Magnon Hybrid System, *Phys. Rev. Lett.* **124**, 117202 (2020).

- [42] H. Huebl, C. W. Zollitsch, J. Lotze, F. Hocke, M. Greifenstein, A. Marx, R. Gross, and S. T. B. Goennenwein, High Cooperativity in Coupled Microwave Resonator Ferrimagnetic Insulator Hybrids, *Phys. Rev. Lett.* **111**, 127003 (2013).
- [43] X. Zhang, C.-L. Zou, L. Jiang, and H. X. Tang, Strongly Coupled Magnons and Cavity Microwave Photons, *Phys. Rev. Lett.* **113**, 156401 (2014).
- [44] L. Bai, M. Harder, Y. Chen, X. Fan, J. Xiao, and C.-M. Hu, Spin Pumping in Electrodynamically Coupled Magnon-Photon Systems, *Phys. Rev. Lett.* **114**, 227201 (2015).
- [45] O. Mosendz, J. E. Pearson, F. Y. Fradin, G. E. W. Bauer, S. D. Bader, and A. Hoffmann, Quantifying Spin Hall Angles from Spin Pumping: Experiments and Theory, *Phys. Rev. Lett.* **104**, 046601 (2010).
- [46] M. Obstbaum, M. Härtinger, H. G. Bauer, T. Meier, F. Swientek, C. H. Back, and G. Woltersdorf, Inverse spin Hall effect in Ni₈₁Fe₁₉/normal-metal bilayers, *Phys. Rev. B* **89**, 060407 (2014).
- [47] L. Bai, M. Harder, P. Hyde, Z. Zhang, C.-M. Hu, Y. Chen, and J. Q. Xiao, Cavity Mediated Manipulation of Distant Spin Currents using a Cavity-Magnon-Polariton, *Phys. Rev. Lett.* **118**, 217201 (2017).
- [48] W. X. Lim, M. Manjappa, P. Pitchappa, and R. Singh, Shaping high-*q* planar Fano resonant metamaterials toward futuristic technologies, *Adv. Opt. Mater.* **6**, 1800502 (2018).
- [49] V. A. Fedotov, M. Rose, S. L. Prosvirnin, N. Papasimakis, and N. I. Zheludev, Sharp Trapped-Mode Resonances in Planar Metamaterials with a Broken Structural Symmetry, *Phys. Rev. Lett.* **99**, 147401 (2007).
- [50] A. Sihvola, Metamaterials in electromagnetics, *Metamaterials* **1**, 2 (2007).
- [51] J. B. Pendry, D. Schurig, and D. R. Smith, Controlling electromagnetic fields, *Science* **312**, 1780 (2006).
- [52] C. Kittel, Excitation of spin waves in a ferromagnet by a uniform rf field, *Phys. Rev.* **110**, 1295 (1958).
- [53] N. Mecking, *A Comprehensive Study of the AMR-Induced Microwave Photovoltage, Photocurrent and Photoresistance in Permalloy Microstrips* (Verlag Dr. Hut, Hamburg, 2008).
- [54] D. F. Walls and G. J. Milburn, *Quantum Optics* (Springer Science & Business Media, Berlin, 2007).
- [55] M. Harder, B. Yao, Y. Gui, and C.-M. Hu, Coherent and dissipative cavity magnonics, *J. Appl. Phys.* **129**, 201101 (2021).
- [56] P.-C. Xu, J. W. Rao, Y. Wang, Y. S. Gui, J. Q. Xiao, X. Jin, and C.-M. Hu, Electrical detection of magnon-photon interactions via an auxiliary spin-wave mode, *Phys. Rev. B* **102**, 014453 (2020).
- [57] T. Holstein and H. Primakoff, Field dependence of the intrinsic domain magnetization of a ferromagnet, *Phys. Rev.* **58**, 1098 (1940).
- [58] J. M. P. Nair, D. Mukhopadhyay, and G. S. Agarwal, Enhanced Sensing of Weak Anharmonicities through Coherences in Dissipatively Coupled Anti-PT Symmetric Systems, *Phys. Rev. Lett.* **126**, 180401 (2021).
- [59] S. Zhang, D. A. Genov, Y. Wang, M. Liu, and X. Zhang, Plasmon-Induced Transparency in Metamaterials, *Phys. Rev. Lett.* **101**, 047401 (2008).
- [60] J. Wang, X. Liu, L. Li, J. He, C. Fan, Y. Tian, P. Ding, D. Chen, Q. Xue, and E. Liang, Huge electric field enhancement and highly sensitive sensing based on the Fano resonance effect in an asymmetric nanorod pair, *J. Opt.* **15**, 105003 (2013).
- [61] J. Qian, J. W. Rao, Y. S. Gui, Y. P. Wang, Z. H. An, and C.-M. Hu, Manipulation of the zero-damping conditions and unidirectional invisibility in cavity magnonics, *Appl. Phys. Lett.* **116**, 192401 (2020).
- [62] Y.-P. Wang, J. W. Rao, Y. Yang, P.-C. Xu, Y. S. Gui, B. M. Yao, J. Q. You, and C.-M. Hu, Nonreciprocity and Unidirectional Invisibility in Cavity Magnonics, *Phys. Rev. Lett.* **123**, 127202 (2019).
- [63] V. Castel, A. Manchec, and J. B. Youssef, Control of magnon-photon coupling strength in a planar resonator/yttrium-iron-garnet thin-film configuration, *IEEE Magn. Lett.* **8**, 1 (2016).
- [64] B. Bhoi, B. Kim, J. Kim, Y.-J. Cho, and S.-K. Kim, Robust magnon-photon coupling in a planar-geometry hybrid of inverted split-ring resonator and YIG film, *Sci. Rep.* **7**, 1 (2017).
- [65] J. T. Hou and L. Liu, Strong Coupling between Microwave Photons and Nanomagnet Magnons, *Phys. Rev. Lett.* **123**, 107702 (2019).
- [66] Y. Li, T. Polakovic, Y.-L. Wang, J. Xu, S. Lendinez, Z. Zhang, J. Ding, T. Khaire, H. Saglam, R. Divan, J. Pearson, W.-K. Kwok, Z. Xiao, V. Novosad, A. Hoffmann, and W. Zhang, Strong Coupling between Magnons and Microwave Photons in On-Chip Ferromagnet-Superconductor Thin-Film Devices, *Phys. Rev. Lett.* **123**, 107701 (2019).
- [67] H. Maier-Flaig, M. Harder, R. Gross, H. Huebl, and S. T. B. Goennenwein, Spin pumping in strongly coupled magnon-photon systems, *Phys. Rev. B* **94**, 054433 (2016).
- [68] X. Zhang, C. Zou, L. Jiang, and H. X. Tang, Superstrong coupling of thin film magnetostatic waves with microwave cavity, *J. Appl. Phys.* **119**, 023905 (2016).
- [69] J. Hausinger and M. Grifoni, Qubit-oscillator system: An analytical treatment of the ultrastrong coupling regime, *Phys. Rev. A* **82**, 062320 (2010).
- [70] B. Z. Rameshti, Y. Cao, and G. E. Bauer, Magnetic spheres in microwave cavities, *Phys. Rev. B* **91**, 214430 (2015).
- [71] B. Hoekstra, R. P. Van Staple, and J. M. Robertson, Spin-wave resonance spectra of inhomogeneous bubble garnet films, *J. Appl. Phys.* **48**, 382 (1977).
- [72] P. Fletcher and R. Bell, Ferrimagnetic resonance modes in spheres, *J. Appl. Phys.* **30**, 687 (1959).
- [73] R. L. White and I. H. Solt, Multiple ferromagnetic resonance in ferrite spheres, *Phys. Rev.* **104**, 56 (1956).
- [74] L. Bai, K. Blanchette, M. Harder, Y. P. Chen, X. Fan, J. Q. Xiao, and C. M. Hu, Control of the magnon-photon coupling, *IEEE Trans. Magn.* **52**, 1 (2016).
- [75] W. Han, S. Maekawa, and X.-C. Xie, Spin current as a probe of quantum materials, *Nat. Mater.* **19**, 139 (2020).